ACES Asian Chemical Editorial Society

doi.org/10.1002/asia.70294

CHEMISTRY AN ASIAN JOURNAL Research Article

www.chemasianj.org

Synergistic Engineering of NiCoFe Layered Hydroxides for Enhanced Energy Storage and Electrocatalytic Water Splitting

Boyao Zhang,[a] Ruiyu Li,[a] Xinxin Zhao,[a] Huiya Zhou,[a] Xin Li,[a] Yibo Wang,*[a] Rongda Zhao,*[a] and Lihua Miao*[b]

The rational design of electrode materials with outstanding energy and power density for supercapacitors (SCc) and high-performance electrocatalysts in alkaline media plays an indispensable role in the application of energy storage and overall water splitting. In this paper, we prepared NiCoFe layered ternary hydroxides (LTH) using a hydrothermal synthesis method. The sample with a Ni/Co/Fe ratio of 1:2:0.5 (Co) exhibited the best performance, achieving a specific capacitance of 860 C g^{-1} at a current density of 1 A·g^{-1}. When assembled into a supercapacitor, it achieved an energy density of 72.3 Wh·kg^{-1} at a power density of 4050 W·kg^{-1}, and after 7200 charge-discharge cycles, the capacity retention rate was 69.2%. For the hydrogen evolution reaction (HER), the overpotential was 100.4 mV at 10 mA·cm^{-2}; in oxygen evolution, the sample with a Ni/Co/Fe ratio of 2:1:1.5 (Ni,Co) showed better performance, presenting an overpotential of 235.3 mV at 50 mA·cm^{-2}. Moreover, when constructing a symmetrical two-electrode system using both ratios of NiCoFe layered hydroxides, the water splitting voltage was only 1.861 V at 100 mA·cm^{-2}. It is hoped that NiCoFe-LDH prepared under appropriate conditions can optimise its applicability as fundamental components for SCc and water-splitting systems.

1. Introduction

As global energy issues become increasingly pressing, interest in alternative and renewable energy sources has continued to grow. The design and development of advanced energy storage systems have thus emerged as a critical research challenge. Among these systems, supercapacitors (SCs) have gained significant attention due to their notable advantages, including high power density, fast charge-discharge capabilities, long cycle life, and environmental friendliness, positioning them as a promising solution for electrochemical energy storage.[1–3] Electrochemical double-layer capacitors (EDLCs) typically employ carbon-based materials as electrode candidates due to their high surface area, enhanced porosity, good chemical stability, mechanical robustness, and low weight.[4] In contrast, pseudocapacitors rely on reversible Faradaic reactions occurring at the electrode surface, which enable significantly higher specific capacitance.[5] Activated carbon (AC) has become the most commonly used electrode material for EDLC. Other carbon materials such as graphene, fullerene, and carbon nanotubes (CNT) are also considered suitable electrode materials for EDLC,[6,7] but they require precise regulation of pore structure, including the ratio and distribution of micropores, mesopores, and macropores, which imposes strict requirements on preparation methods and increases costs. The electrochemical performance of hybrid supercapacitors (HSCs) is determined by the efficacy of battery-type Faradaic electrode materials. Therefore, the design and synthesis of advanced electrode materials with ideal structures are considered crucial factors in HSC development. Among various battery-type Faradaic electrode materials, nanostructured binary transition metal nickel-cobalt oxides (Ni, CO) have recently been recognized as promising advanced electrode materials for HSCs.[8–10] Sustainable hydrogen is also considered an ideal candidate to replace fossil fuels. Water electrolysis provides an effective method for large-scale production of pure hydrogen.[11,12] The overall water electrolysis process consists of two half-reactions: the oxygen evolution reaction (OER) at the anode and the hydrogen evolution reaction (HER) at the cathode. The complete reaction pathway of water electrolysis is governed by the kinetics of these two half-reactions, which are coupled at the electrode–electrolyte interface. Since the thermodynamics of this process are non-spontaneous ($\Delta G > 0$), external electrical energy must be supplied to overcome the Gibbs free energy barrier. Therefore, the smaller the overpotential required, the closer the system operates to the theoretical decomposition voltage (1.23 V), thereby enabling more efficient water splitting. This electron transfer process occurring at the electrode-electrolyte interface is referred to as the electrochemical OER. Due to the involvement of multi-electron transfer processes, anode water oxidation remains a bottleneck in water electrolysis; hence, efficient electrocatalyst materials are needed to accelerate kinetics and achieve high current densities at minimal overpotential.[13,14] At present, the widespread application of electrochemical water splitting is

[a] B. Zhang, R. Li, X. Zhao, H. Zhou, X. Li, Y. Wang, R. Zhao
School of Materials Science and Engineering, Liaoning University of Technology, Jinzhou, Liaoning 121000, China
E-mail: clwangyibo@lnut.edu.cn
Rongdazhaoln@126.com

[b] L. Miao
School of Medical Information Engineering, Shenyang Medical College, Shenyang, Liaoning 110043, P. R. China
E-mail: miaolihua@163.com

Supporting information for this article is available on the WWW under https://doi.org/10.1002/asia.70294

constrained by the high cost of precious metal catalysts. An important avenue of research involves developing alternative non-precious metal-based electrode materials, particularly those based on transition metals. Transition metal layered double hydroxides (LDHs) and their composite catalysts are promising candidates due to their low cost and inherently large specific surface areas. These properties facilitate rapid interaction with the electrolyte and enhance charge transfer rates, leading to the creation of highly active sites with increased accessibility to internal atoms. Nonetheless, achieving significant performance improvements requires further strategic enhancements, such as optimizing structures and controlling defects. Such strategies are crucial for driving substantial advancements in water-splitting technologies.[15–18] Nickel foam (NF) exhibits excellent electrochemical performance due to its 3D porous structure and robust framework. This structure not only provides abundant active sites for uniform catalyst loading and enhances structural stability, but also improves the adhesion between the catalyst and the substrate, effectively preventing catalyst detachment or deactivation during long-term operation. Therefore, NF serves as an ideal substrate for high-performance electrochemical devices.[19] Battery-type transition metal oxides/hydroxides possess two crystal structures, with layered hydroxides exhibiting high pseudocapacitance performance, high redox activity, and environmental friendliness, making them very promising materials for energy storage applications.[20,21] Synthesizing layered ternary hydroxides (LTH) to enhance their electrocatalytic activity has been recognized as an effective approach in recent years. Furthermore, the synergistic modulation of ion incorporation and composite architectures offers a promising strategy to simultaneously overcome critical challenges, including poor electrical conductivity, structural instability, and sluggish ion diffusion. By leveraging these strategies, it is possible to achieve an optimal balance of high capacity, long cycle life, and superior rate capability.[22–25] Layered mixed hydroxides similar to hydrotalcite materials (HTs) containing transition metals (Ni, Co, Fe) are among the most promising candidates for OER electrocatalysts, and their performance is mainly related to important surface areas and the availability of M-OH groups.[26,27] Ni/Fe LDH is one of the materials with relatively high electrocatalytic activity.[28] In LDHs, the combination of Ni and Co binary composites, due to their excellent redox reversibility and relatively high capacity, represents a promising class of active materials. Numerous studies have shown that the molar ratio of active Ni to Co significantly affects the structure, morphology, and capacitive performance of NiCo-LDH.[29–32] Liu et al.[33] synthesized NiCoFe LDHs through a solvothermal method, which exhibited a specific capacitance of 490 $C{\cdot}g^{-1}$ at a current density of 2 $A{\cdot}g^{-1}$ and good cycling stability, retaining 90.9% capacitance after 1000 cycles. Sivakumar et al.[34] reported that the NiCo carbonate hydroxide supercapacitor they fabricated achieved an energy density of 50.1 Wh kg^{-1} at a specific power of 805.6 W kg^{-1}. Therefore, we chose to synthesize a series of LTH with different ratios of Ni, Co, and Fe to explore the optimal synthesis ratio that exhibits excellent electrochemical and electrocatalytic performance.

This study focuses on the fundamental exploration of nickel-cobalt-iron LDHs (NiCoFe-LDH). Our primary aim was to maximize their electrochemical performance in both energy storage and electrocatalytic conversion by precisely controlling the ratios of the three metal ions: Ni, Co, and Fe. To achieve this, we designed and executed a series of rigorous comparative experiments, systematically investigating how varying elemental ratios influence the structural characteristics of NiCoFe-LDH materials and their profound impact on performance in SCc, as well as in hydrogen evolution and OERs. Experimental results indicate that in supercapacitor applications, the sample with a Ni:Co:Fe ratio of 1:2:0.5 (Co) exhibits the most outstanding electrochemical performance, achieving a specific capacitance of 860 $C{\cdot}g^{-1}$ at a current density of 1 $A{\cdot}g^{-1}$. When assembled into a supercapacitor, it achieves an energy density of 72.3 $Wh{\cdot}kg^{-1}$ at a power density of 4050 $W{\cdot}kg^{-1}$. Additionally, this sample demonstrates remarkable performance in HER catalytic activity tests, showing a low overpotential of 100.4 mV to achieve a current density of −10 $mA{\cdot}cm^{-2}$ and a Tafel slope of 71.2 mV dec^{-1} in 1 M alkaline potassium hydroxide solution. Regarding OER performance, when the Ni:Co:Fe ratio is 2:1:1.5 (Ni, Co), the sample shows an overpotential of only 235.3 mV at a current density of 50 $mA{\cdot}cm^{-2}$ and an active site density of 0.186 $mF{\cdot}cm^{-2}$. This study provides both experimental strategies and theoretical insights for exploring catalysts with enhanced activity and stability.

2. Experimental Section

2.1. Materials

Iron nitrate [$Fe(NO_3)_3$, 99%], cobalt nitrate hexahydrate [$Co(NO_3)_2{\cdot}6H_2O$, 99%], nickel nitrate hexahydrate [$Ni(NO_3)_2{\cdot}6H_2O$, 99%], ammonium fluoride (NH4F, 96%), urea (H2NCONH2, 99.5%), potassium hydroxide (KOH), absolute ethanol (C_2H_6O, 99.5%), and NF were all used as received. All chemical reagents were of analytical grade and purchased from Sigma-Aldrich Chemical Company without further purification. The preparation of all catalysts was carried out in a Teflon-lined stainless steel autoclave.

2.2. Pretreatment of NF

The NF substrate was first pretreated using an ultrasonic cleaner. Specifically, the NF was sequentially immersed in absolute ethanol for 30 min and then in deionized water (DI water) for another 30 min; this process was repeated three times. After the cleaning was completed, the NF was placed in a 60 °C oven and dried for over 24 h to ensure that there were no residual solvents on the surface.

2.3. Preparation of NiCoFe-LDH

As shown in Scheme 1, a specified ratio of nickel nitrate hexahydrate ($Ni(NO_3)_2{\cdot}6H_2O$), cobalt nitrate hexahydrate ($Co(NO_3)_2{\cdot}6H_2O$), and ferric nitrate nonahydrate ($Fe(NO_3)_3{\cdot}9H_2O$), along with 6 mmol of urea and 2 mmol of ammonium fluoride, was dissolved in 50 mL of DI water. The mixed solution was magnetically stirred for 45 min to ensure complete dissolution and homogeneity. Subsequently, the pretreated NF was vertically immersed into the as-prepared solution and transferred to a Teflon-lined stainless steel autoclave for the hydrothermal reaction. The reaction was carried out at 120 °C for 6 h. After the reaction was complete, the autoclave was allowed to cool naturally to room temperature. The sample was then removed and

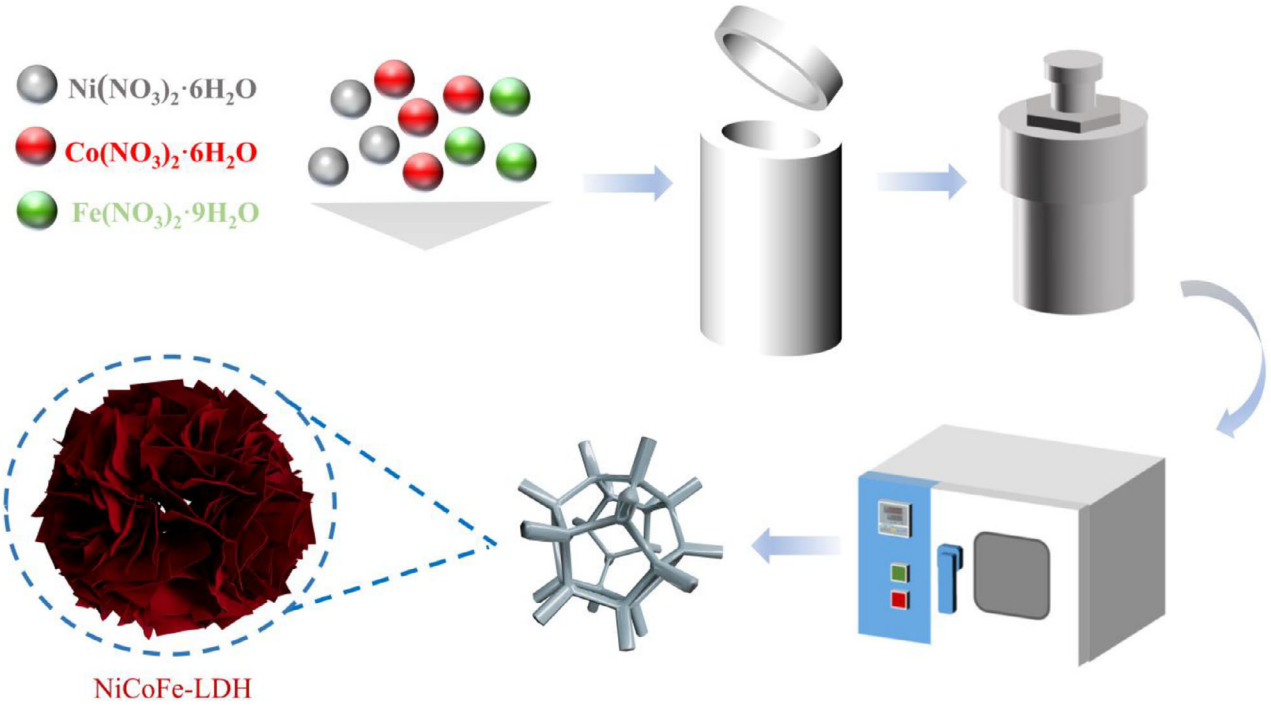

Scheme 1. Schematic illustration of synthesizing of NiCoFe-LDH foam nickel.

sequentially washed three times each with ethanol and deionized water. Finally, the sample was dried at 60 °C for at least 12 h, resulting in the NiCoFe-LDH/NF composite electrode material.

2.3.1. Experimental Design for Comparing Reaction Concentrations

1. Fixed Ni Content Group: Keeping the molar amount of Ni constant while adjusting the molar ratios of Co and Fe. The specific ratios are Ni:Co:Fe = 2:1:1, 2:1:0.5, 2:1.5:0.5, 2:0.5:1, and 2:0.5:1.5, denoted as 2:1:1(Ni), 2:1:0.5(Ni), 2:1.5:0.5(Ni), 2:0.5:1(Ni), and 2:0.5:1.5(Ni), respectively.
2. Fixed Co Content Group: Keeping the molar amount of Co constant while adjusting the molar ratios of Ni and Fe. The specific ratios are Ni:Co:Fe = 1:2:1, 1:2:0.5, 1.5:2:0.5, 0.5:2:1, and 0.5:2:1.5, denoted as 1:2:1(Co), 1:2:0.5(Co), 1.5:2:0.5(Co), 0.5:2:1(Co), and 0.5:2:1.5(Co), respectively.
3. Fixed Ni and Co Content Group: Keeping the molar ratio of Ni to Co constant while adjusting only the molar amount of Fe. The specific ratios are Ni:Co:Fe = 2:1:0.25, 2:1:0.5, 2:1:0.75, 2:1:1, and 2:1:1.5, denoted as 2:1:0.25(Ni,Co), 2:1:0.5(Ni,Co), 2:1:0.75(Ni,Co), 2:1:1(Ni,Co), and 2:1:1.5(Ni,Co), respectively.

Subsequently, the best-performing samples from each group were subjected to electrocatalytic testing and characterization. All samples were prepared under identical conditions (120 °C for 6 h) to ensure comparability and reliability of the experimental results. The products after reaction were processed according to the aforementioned cleaning and drying procedures for subsequent characterization and electrochemical performance testing.

2.4. Material Characterization and Electrocatalytic Performance Characterization

The crystal structure of the prepared samples was characterized by X-ray diffraction (XRD, Shimadzu-7000, Cu Kα) over a range of 10° to 90° with a scanning speed of 8°/min. The micro-morphological changes of the prepared samples were characterized using scanning electron microscopy (SEM, Gemini 300–71–31). X-ray photoelectron spectroscopy (XPS, ESCALAB 250 with Al Kα radiation) was employed to determine the surface chemical states, elemental valence states, and qualitative and quantitative information of the elements in the material.

Electrochemical tests were conducted using a potentiostat (CHI 760E) in a three-electrode configuration with 3 M KOH solution as the electrolyte. Each sample, with a diameter of 10 mm, was held by a stainless steel electrode clip serving as the working electrode, while a platinum plate and a Hg/HgO electrode served as the counter and reference electrodes, respectively. For electrocatalytic performance testing, 1 M KOH (pH = 13.7) alkaline solution was used as the electrolyte, with Hg/HgO as the reference electrode, a graphite rod and Pt electrode as the counter electrodes, and the prepared samples (0.5 cm × 0.5 cm) as the working electrode. Linear sweep voltammetry (LSV) curves were corrected for 90% IR compensation and converted to the reversible hydrogen electrode (RHE) according to the Nernst equation $E_{RHE} = E_{Hg/HgO} + 0.059 \times PH + 0.098$. The OER overpotential was calculated as $\eta = E_{RHE} - 1.23$ V. The areal specific capacitance was calculated from the galvanostatic charge-discharge (GCD) curves using the formula:

$$C_A = \frac{I\Delta t_d}{S} \quad (1)$$

where I and Δtd represent the set current value and discharge time, respectively, and S denotes the geometric area of the electrode.

2.5. Preparation and Performance Testing of the Assembled Electrolyte

2.5.1. Preparation of Electrodes and Electrolyte

= For the asymmetric supercapacitor assembly, AC was used as the cathode material, while the anode material consisted of NiCoFe-

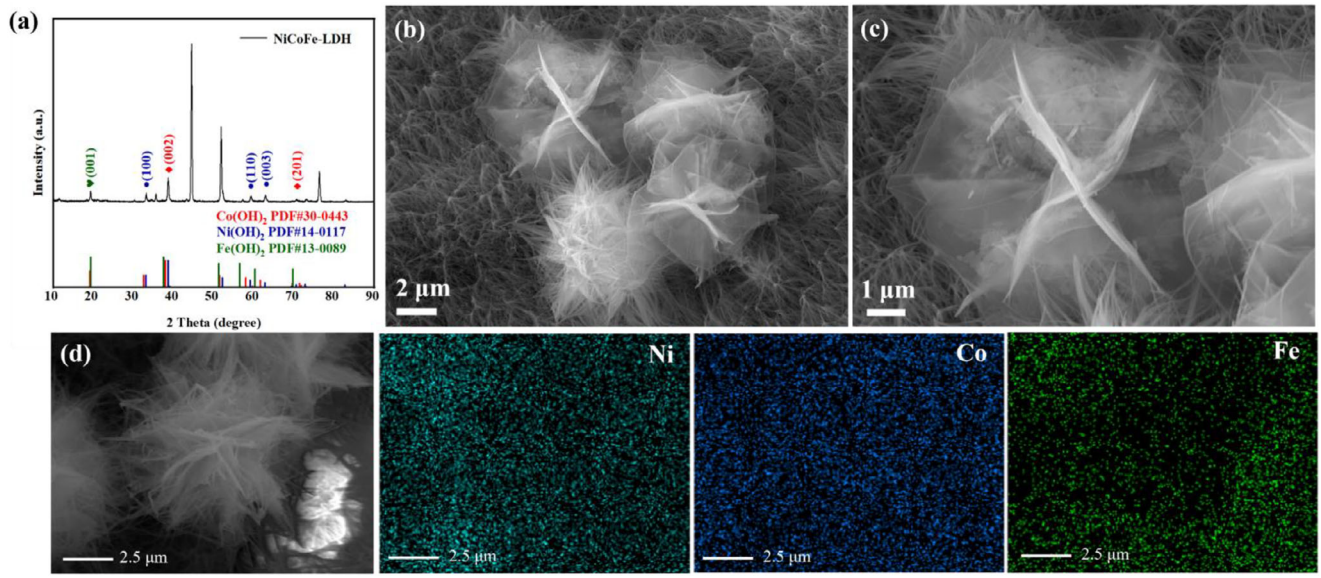

Figure 1. Characterization of morphology and structure a) XRD patterns of NiCoFe-LDH Sample and its precursor, b, c) SEM images of NiCoFe-LDH. d) Elemental mapping of NiCoFe-LDH samples.

LDH supported on NF. Poly(vinyl alcohol)-KOH (PVA-KOH) gel was employed as the electrolyte. Electrolyte Preparation: The preparation method for the electrolyte remained consistent: 2 g of PVA was dissolved in 20 mL of DI water, and 2 g of KOH was dissolved in 5 mL of DI water. These solutions were stirred at 80 °C until they became clear and transparent. Cathode (AC Electrode) Fabrication: For the AC electrode, a mixture was prepared at a mass ratio of 8:1:1 using AC, acetylene black, and poly(vinylidene fluoride) to form a slurry. This slurry was then coated onto NF and dried at 60 °C for 24 h to form the final electrode. Gel Electrolyte Synthesis: The process for synthesizing the gel electrolyte followed the original steps: 2 g of PVA was dissolved in 15 mL of DI water and stirred at 80 °C for 30 min until complete dissolution. While continuously stirring, concentrated KOH solution (with a concentration of 0.4 g/mL) was added dropwise until no more bubbles were observed, indicating thorough mixing of the two solutions.

2.5.2. Performance Testing

To comprehensively evaluate the electrochemical performance of the electrodes and SCc during long-term cycling, a LAND battery testing system (CT2001A) was employed for durability testing. The energy density (E, mWh·cm^{-2}) and power density (P, mW·cm^{-2}) were calculated using the following formulas:

$$E = \frac{C_A \Delta V^2}{7200} \quad (2)$$

$$P = \frac{3600E}{\Delta t} \quad (3)$$

3. Results and Discussion

Figure 1a shows the XRD diffraction pattern of the NiCoFe-LDH samples. As can be observed from the figure, the sample exhibits distinct diffraction peaks at $2\theta = 21.6°$, 34.7°, 38.8°, 58.5°, 62.9°, and 69.8°, corresponding to the (001), (100), (002), (110), (003), and (201) crystal planes of the LTH structure, respectively. These characteristic peaks match well with the diffraction peak positions of $Co(OH)_2$ (PDF#30–0443), $Ni(OH)_2$ (PDF#14–0117), and $Fe(OH)_3$ (PDF#13–0089) in standard PDF cards, indicating that the NiCoFe-LDH material with a layered double hydroxide structure has been successfully synthesized. The presence of (001) and (003) peaks confirms the typical layered structure of the material, while the (110) peak reflects the arrangement of metal-oxygen octahedra within the layers.[35] Figures 1b,c present SEM images at different magnifications, clearly illustrating the micro-morphology of NiCoFe-LDH. It can be seen that NiCoFe-LDH exhibits a characteristic flower-like 3D layered structure composed of numerous interwoven nanosheets. Figure 1b indicates that these flower-like structures have diameters of approximately 1–2 μm, while the high-magnification SEM image in Figure 1c further reveals that these structures are made up of ultra-thin nanosheets with thicknesses of about 10–20 nm interweaving with each other. This unique 3D open-layered structure not only provides abundant active sites but also facilitates electrolyte penetration and rapid ion transport, which are key structural factors contributing to the excellent electrochemical performance of this material. XPS analysis was further employed to investigate the surface elemental composition and oxidation states of the NiCoFe-LDH 1:2:0.5 (Co) sample. As shown in the full spectrum in Figure 2a, distinct peaks corresponding to C 1 s, Fe 2p, Co 2p, and Ni 2p are clearly observed, confirming the presence of carbon, iron, cobalt, and nickel as the main elements in the catalyst. The pie chart on the right presents the atomic percentage of each element: Ni (14.9%), Co (17.4%), and Fe (7%). The Ni 2p spectrum (Figure 2b) exhibits two main peaks at 856.3 eV and 873.8 eV, corresponding to the Ni $2p_{3/2}$ and Ni $2p_{1/2}$ levels, respectively, with a spin-orbit splitting energy of 17.5 eV. These peaks clearly indicate the presence of $Ni(OH)_2$ phase in the sample, where nickel is in the +2 oxidation state.

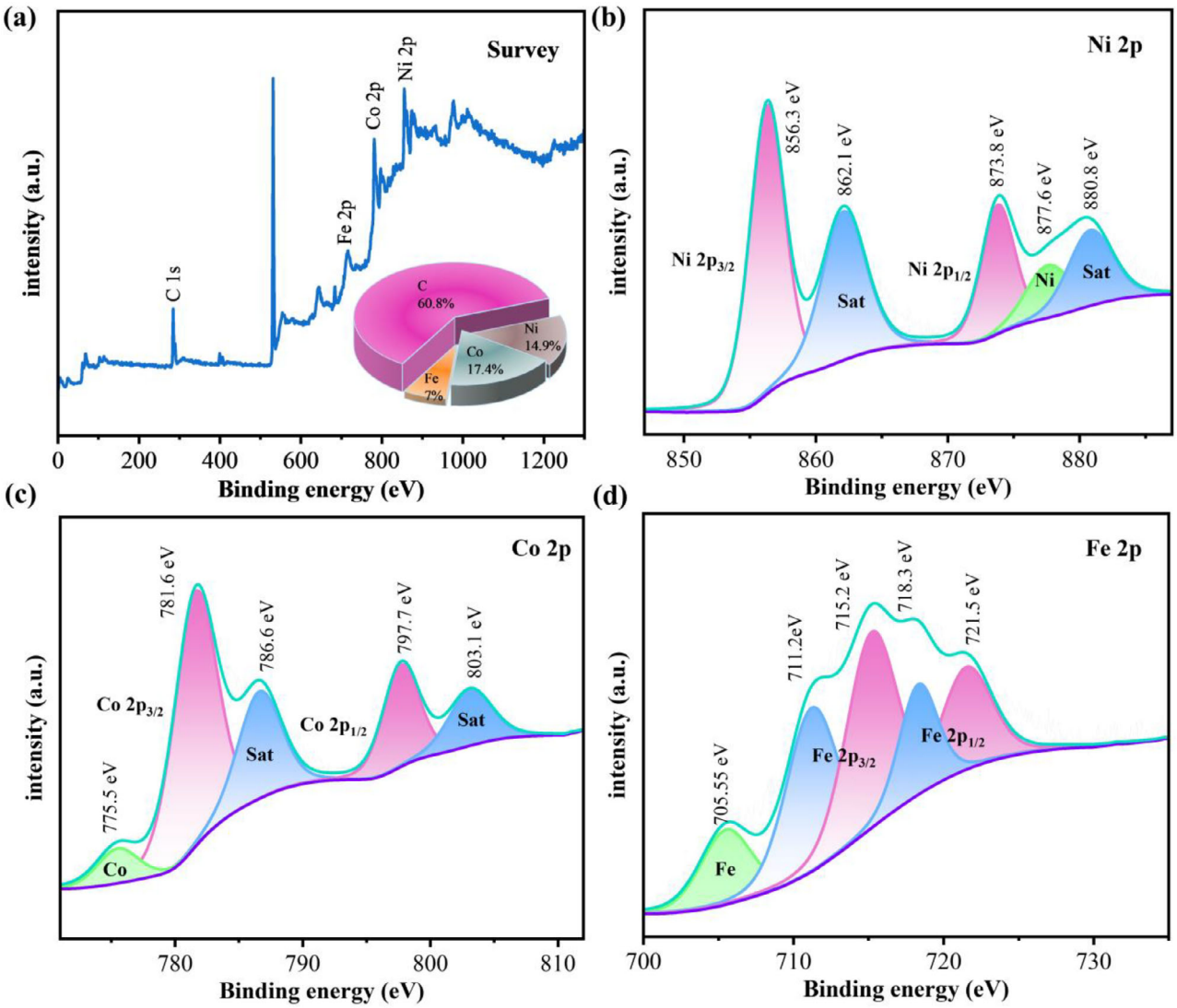

Figure 2. Structure characterization of the as-prepared electrocatalysts (1:2:0.5 (Co)) a) XPS full spectra b) Ni 2p c) Co 2p d) Fe 2p.

In addition, shake-up satellite peaks observed at around 862.1 eV and 880.8 eV further support the existence of Ni (II)[36] The peak at 877.6 eV can be attributed to the characteristic state of Ni. The Co 2p spectrum (Figure 2c) displays two dominant peaks at 781.6 eV and 797.7 eV, corresponding to the Co $2p_{3/2}$ and Co $2p_{1/2}$ states, respectively, which are typically associated with Co (II) and Co (III) oxidation states. Two satellite peaks at 786.6 eV and 803.1 eV further confirm the presence of Co (II). Notably, a peak at 775.5 eV is attributed to metallic Co^0,[37] suggesting the presence of a small amount of elemental cobalt in the sample. Therefore, cobalt exists in the sample in three oxidation states: +2, +3, and 0. In the Fe 2p spectrum (Figure 2d), two main peaks are observed at 711.2 eV and 718.3 eV, corresponding to the Fe $2p_{3/2}$ and Fe $2p_{1/2}$ levels, respectively. These peaks are typically assigned to Fe (III) species, which is the common oxidation state of iron in LDH materials[38] Additionally, a peak at 705.55 eV is attributed to metallic Fe^0, indicating the possible presence of trace amounts of zero-valent iron. In summary, iron exists in the sample in both +3 and 0 oxidation states, with Fe (III) being the dominant form.

Figure 3(a⁻e) presents the cyclic voltammetry (CV) curves of NiCoFe-LDH samples with varying Co/Fe molar ratios (with fixed Ni content) in 1 M KOH electrolyte. It can be observed that all samples exhibit good pseudocapacitive characteristics, showing distinct redox peaks at different scan rates, indicating that the charge storage process is primarily dominated by a pseudocapacitive mechanism.[39] Notably, the sample with a ratio of 2:1.5:0.5 (Ni) (Figure 3c) exhibits the highest current response at the same scan rate, and the area enclosed by the CV curve is significantly larger than those of other compositions, suggesting higher specific capacitance and superior electrochemical activity. Figures 3(f–j) show the GCD curves of various samples at different current densities. The 2:1.5:0.5 (Ni) sample (Figure 3h) displays the longest charge-discharge time (1557 s) at a current density of 1 $A{\cdot}g^{-1}$, corresponding to a specific capacitance of 753 $C{\cdot}g^{-1}$. This confirms its excellent

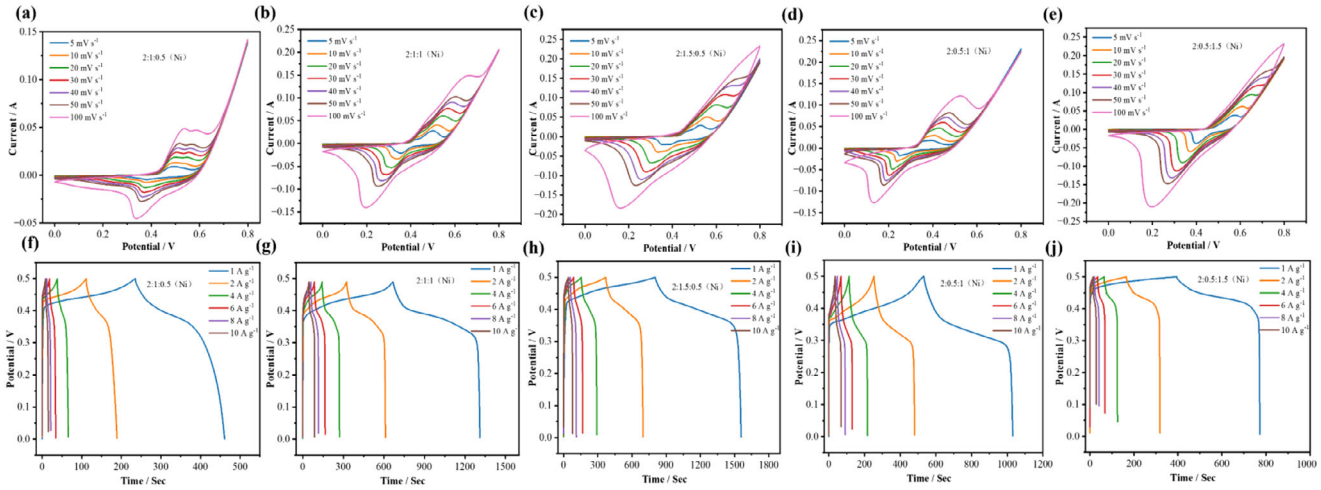

Figure 3. Electrochemical performance of as-prepared electrodes a–e) CV curves of the Ni-fixed group, f–j) GCD curves of the Ni-fixed samples.

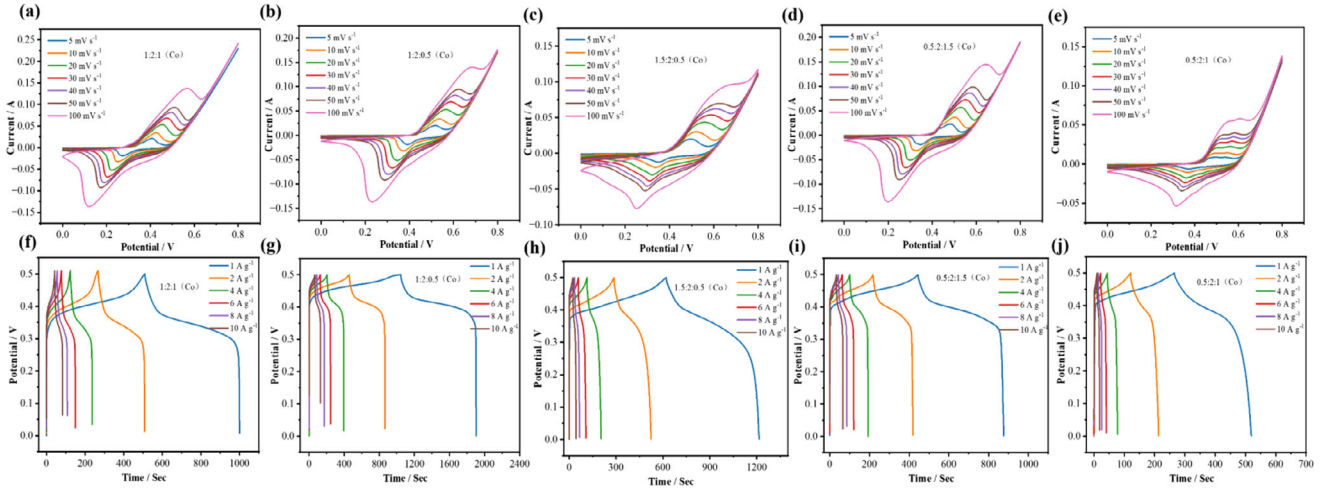

Figure 4. Electrochemical performance of as-prepared electrodes a–e) CV curves of the Co-fixed group, f–j) GCD curves of the Cofixed samples.

energy storage performance. Among the samples with fixed Ni content, the 2:1.5:0.5 (Ni) composition demonstrates the best electrochemical performance. This superior performance is mainly attributed to the optimal Co/Fe ratio, which synergistically regulates the microstructure and electrochemical activity of the material, enhancing its charge storage capacity and reaction kinetics. Additionally, the 2:1.5:0.5 (Ni) composition provides an important reference for subsequent performance optimization and mechanistic studies.

Figure 4(a–e) show the cyclic voltammetry curves of NiCoFe-LDH samples with varying Ni/Fe molar ratios (with fixed Co content) in 1 M KOH electrolyte. All samples exhibit distinct redox peaks at different scan rates, indicating good pseudocapacitive characteristics. Among the compositions, the 1:2:0.5 (Co) sample (Figure 4b) displays the highest current density at the same scan rate, and the area enclosed by the CV curve is significantly larger than those of other samples, suggesting superior specific capacitance and electrochemical activity. Figure 4(f–j) present the GCD curves of these samples at various current densities. The 1:2:0.5 (Co) sample (Figure 4g) shows the longest charge-discharge time (1904.7 s) at a current density of 1 $A \cdot g^{-1}$, corresponding to a specific capacitance of 860 $C \cdot g^{-1}$. This further confirms its excellent energy storage performance. Additionally, the charge-discharge curves of this sample exhibit good symmetry and clear voltage plateaus, indicating favorable reversibility and rate capability. In summary, the test results demonstrate that the 1:2:0.5 (Co) sample exhibits the best electrochemical performance among the samples with fixed Co content. This superior performance is primarily attributed to the optimal Ni/Fe ratio, which effectively regulates the microstructure and charge transfer efficiency of the material, thereby enhancing its electrochemical activity and cycling stability. Therefore, the 1:2:0.5 (Co) composition provides an important reference for further optimization of LDH-based energy storage materials.

Figure 5(a–e) display the cyclic voltammetry curves of NiCoFe-LDH samples with fixed Ni and Co content (2:1:x, where x represents the molar ratio of Fe) in 1 M KOH electrolyte. Systematic comparison and analysis indicate that the sample

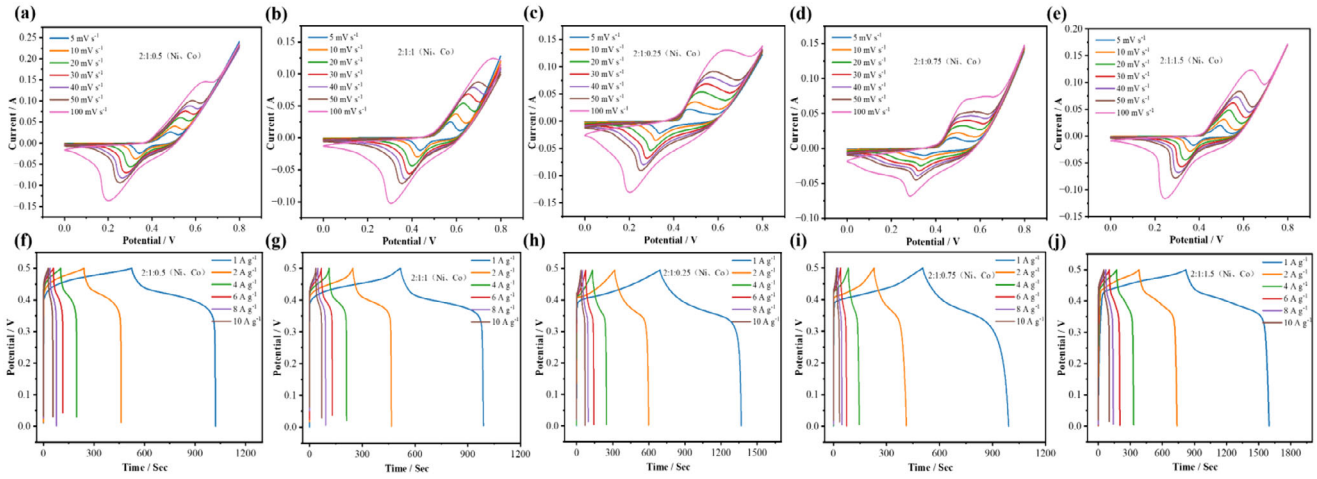

Figure 5. Electrochemical performance of aAs-prepared electrodes a–e) CV curves of the Ni\Co-fixed group, f–j) GCD curves of the Ni\Co-fixed samples.

with a ratio of 2:1:1.5 (Ni, Co) exhibits the most superior electrochemical performance. As seen in the CV curve (Figure 5e), the 2:1:1.5 (Ni, Co) sample shows the highest redox peak current density and the largest enclosed area at various scan rates (5–100 mV/s). The redox peaks are symmetric and stable in position, indicating the highest electrochemical activity and optimal reversibility. The redox peaks observed in the potential range of 0.2–0.6 V correspond to reversible redox reactions of Ni^{2+}/Ni^{3+} and Co^{2+}/Co^{3+}.[40] As the scan rate increases, the peak current density increases while maintaining good peak shape, demonstrating excellent charge transport capability and rate performance. Figures 5(f–j) present the GCD curves of these samples at different current densities. The GCD curve of the 2:1:1.5 (Ni,Co) sample (Figure 5j) further confirms its superiority. At a current density of 1 $A{\cdot}g^{-1}$, it exhibits the longest charge-discharge time (1597.7 s), corresponding to a specific capacitance of 777 $C{\cdot}g^{-1}$. The superior electrochemical performance of the 2:1:1.5 (Ni,Co) sample is primarily attributed to its optimized iron content (Fe content of 1.5). Under fixed nickel (Ni) and cobalt (Co) contents at a 2:1 ratio, the strategic incorporation of an appropriate amount of iron significantly enhanced the properties of the ternary metal hydroxide. The addition of iron fostered a synergistic effect among the nickel, cobalt, and iron ions, thereby increasing the overall electrochemical active sites within the material. Concurrently, the optimized iron content refined the material's crystal structure, leading to improved electronic and ionic transport pathways and, consequently, reduced charge transfer resistance. Furthermore, the introduction of iron optimized the electronic structure at the electrode/electrolyte interface, which accelerated charge transfer kinetics. These collective enhancements enabled the 2:1:1.5 (Ni,Co) sample to exhibit superior electrochemical activity, excellent reversibility, outstanding charge transport capability, and a remarkable specific capacitance within its series. Therefore, in the design and fabrication of high-performance ternary metal hydroxide electrode materials, precise control over the iron content is a critical strategy for achieving enhanced electrochemical properties.

Figure 6a illustrates the cyclic voltammetry curves of the three best-performing compositions: 2:1.5:0.5(Ni), 1:2:0.5(Co), and 2:1:1.5(Ni,Co) in 1 M KOH electrolyte. It is evident that the 1:2:0.5(Co) sample exhibits the highest redox peak current density and the largest enclosed area within the same potential range, indicating higher charge storage capability and superior electrochemical activity. Figure 6b shows the GCD curves of these three materials at various current densities. The 1:2:0.5(Co) sample displays the longest charge-discharge time and the most pronounced voltage plateaus, further confirming its higher specific capacitance and excellent rate performance. Figure 6c presents the Nyquist plots from electrochemical impedance spectroscopy (EIS). The 1:2:0.5(Co) sample has the smallest semicircle diameter in the high-frequency region, indicating the lowest interface charge transfer resistance (R_{ct}) and the highest charge transfer efficiency, which facilitates rapid electrochemical reaction kinetics. In the low-frequency region, the impedance can be referenced by the following formula:[41]

$$Z = R_s + R_{ct} + \sigma w \omega^{-1/2} \quad (4)$$

where σw represents the Warburg factor and ω represents the angular frequency. Z is attributed to the diffusion resistance of OH^-.

Figure 6d compares the specific capacitance trends of the three materials at different current densities. The 1:2:0.5(Co) sample exhibits a specific capacitance of 860 $C{\cdot}g^{-1}$ at a current density of 1 $A{\cdot}g^{-1}$. Compared to other samples, the 1:2:0.5(Co) sample shows a faster OH^- ion transport rate and maintains the highest specific capacitance across all current densities with a relatively slower decay rate. Figure 6e presents the b-value analysis for the three materials. The upper three lines represent the oxidation peaks, with the 1:2:0.5(Co) sample having a b-value of 0.67; the lower three lines represent the reduction peaks, with a b-value of 0.01. A b-value closer to 1 indicates that the process is dominated by surface capacitance, while a value closer to 0.5 suggests diffusion-controlled processes. The higher b-value of the 1:2:0.5(Co) sample indicates faster reaction kinetics and stronger pseudocapacitive characteristics. Figure 6f analyzes

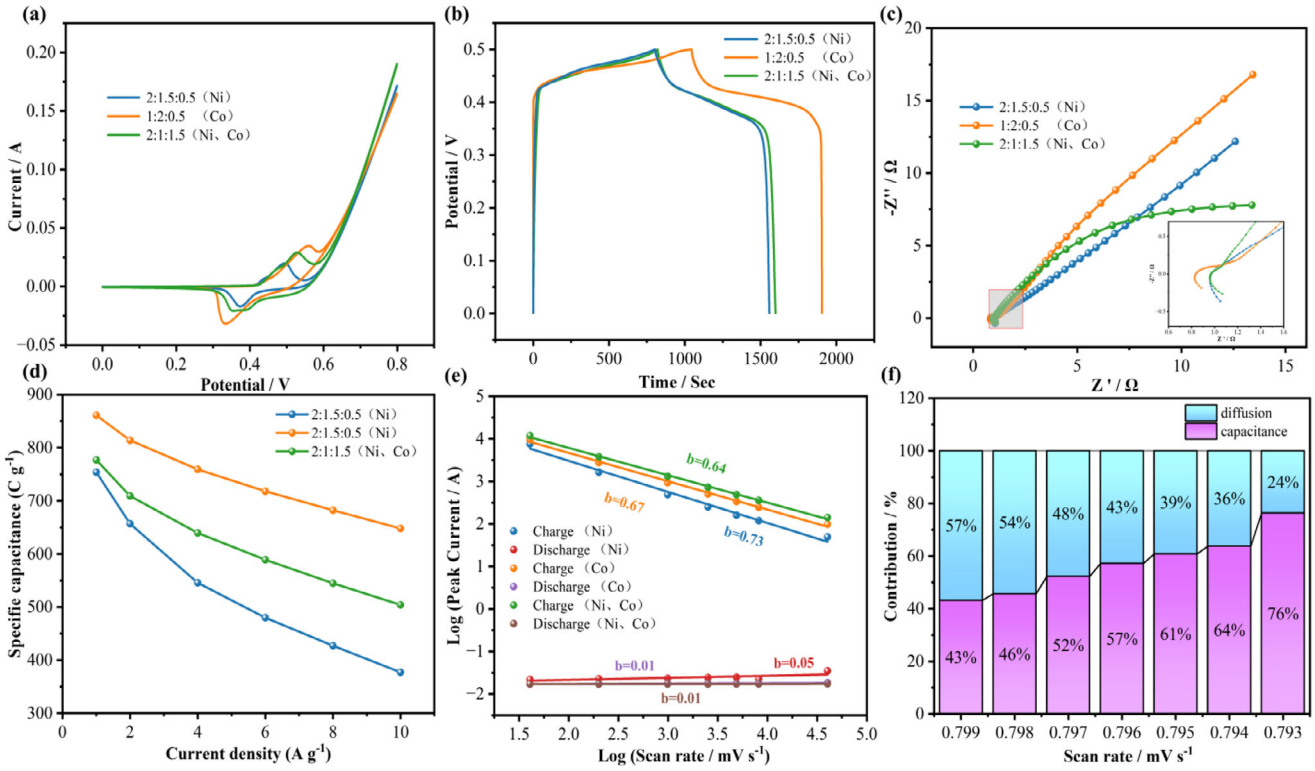

Figure 6. Electrochemical performance of the NiCoFe-LDH electrode prepared under the three optimal Ni/Co/Fe molar ratios: a) CV curves, b) GCD curves, c) EIS plots, d) specific capacitance plots, e) b-value plots, f) contribution of diffusion-controlled and surface capacitance at various scan rates.

the contributions of diffusion and surface capacitance to the 1:2:0.5(Co) sample's performance at various scan rates. As the scan rate increases, the contribution from surface capacitance gradually rises from 43% to 76%, while the diffusion-controlled contribution decreases accordingly. This indicates that at higher scan rates, electrode reactions are more dependent on surface pseudocapacitive processes, which facilitates rapid charging and discharging.

To evaluate the electrochemical performance of the 1:2:0.5(Co) material, a supercapacitor was assembled using it as the positive electrode and AC as the negative electrode, followed by systematic testing. As shown in Figure 7a, the 1:2:0.5(Co)/AC supercapacitor exhibits distinct redox peaks at different operating voltages, indicating typical pseudocapacitive behavior. With increasing voltage, the area enclosed by the CV curves increases, reflecting enhanced capacitance. The CV curves at various scan rates (Figure 7b) maintain their shape with only slight shifts in peak current, confirming excellent reversibility. Figure 7c shows that the specific capacitance decreases with increasing current density from 1 to 5 A·g^{-1}, which is consistent with the characteristics of pseudocapacitive materials. The EIS curve in Figure 7d reveals a small semicircle in the high-frequency region, indicating low charge transfer resistance and favorable reaction kinetics. The Ragone plot (Figure 7e) demonstrates that the device delivers an energy density of 72.3 Wh·kg^{-1} at a power density of 4050 W·kg^{-1}, the energy density of this sample is higher than that of other reported sample devices. Table 2 compares the energy and power densities of the NiCoFe-LDH-based supercapacitor with various Ni/Co-based electrode materials reported in the literature. The results show that the NiCoFe-LDH electrode fabricated in this study delivers a high energy density of 72.3 Wh kg^{-1} at a power density of 4050 W kg^{-1}, outperforming other Ni/Co-based materials such as La@$NiCoFe_2O_4$ (42.2 Wh kg^{-1}), NiCo-PBA (42.16 Wh kg^{-1}), NiCoP (16.72 Wh kg^{-1}), and $NiCo_2O_4$-Mn (19.9 Wh kg^{-1}). In addition, although NiCoZnS@NiCoFe-LDH also exhibits a relatively high energy density of 66.25 Wh kg^{-1}, its power density is significantly lower. This comparative analysis suggests that constructing a multi-component composite structure, particularly by introducing a third metallic element (e.g., Fe) into the NiCo system, can serve as an effective strategy to enhance the electrochemical performance of electrode materials. Figure 7f shows the capacity retention of the 1:2:0.5 (Co)/AC supercapacitor after 7200 charge-discharge cycles, with a retention rate of 69.2%. The inset displays the electrochemical impedance spectroscopy (EIS) spectra before and after cycling. Prior to cycling, the low-frequency region of the Nyquist plot is closer to the Y-axis (i.e., smaller Z' values), with a slope approaching vertical, indicating lower diffusion impedance within the electrode material. After cycling, there is a slight increase in Z' values, suggesting that charge transfer at the electrode/electrolyte interface has become more challenging. This can be attributed to the formation of a surface layer on the electrode that hinders ion diffusion. Despite a capacity decay of 30.8%, the retention rate observed over 7200 cycles can be considered relatively moderate, given the high number

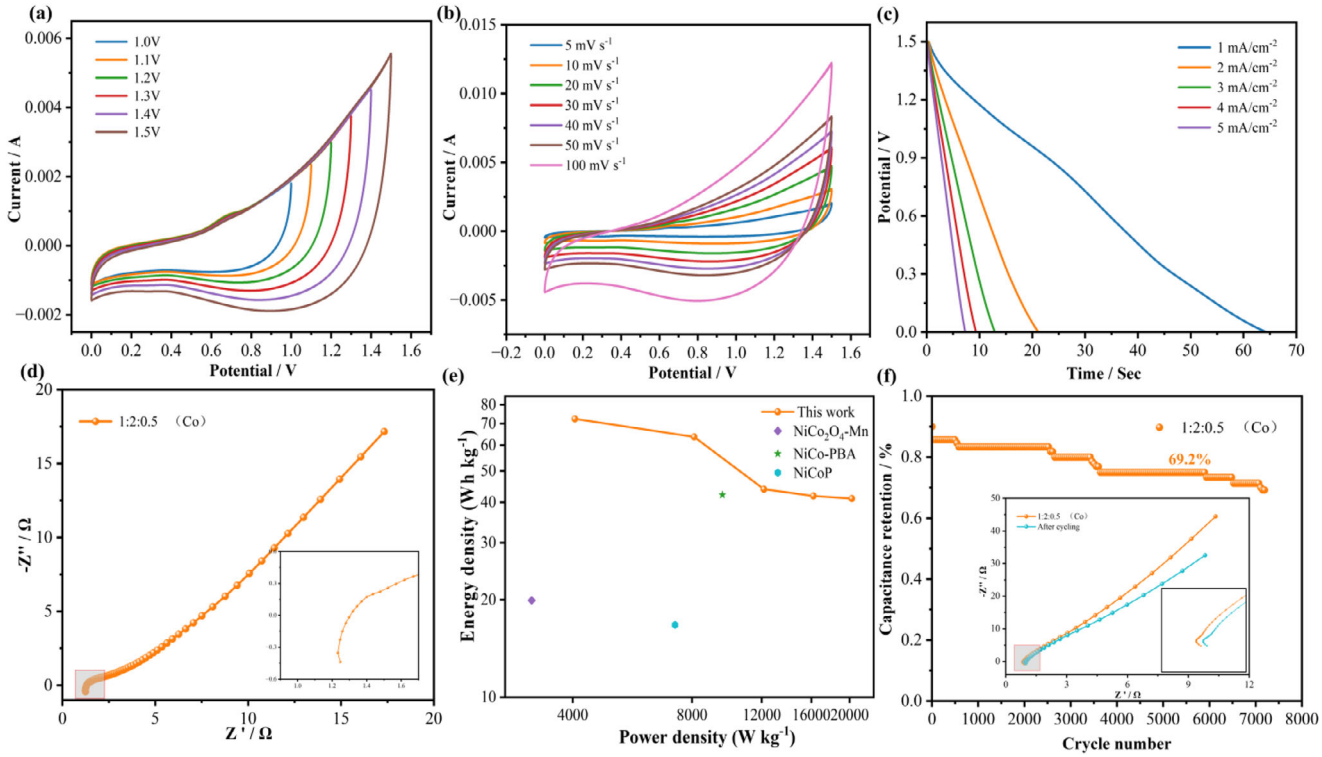

Figure 7. Electrochemical curves of the ASC device assembled with the 1:2:0.5 (Co) material: a) CV curves at different operating voltages, b) CV curves at different scan rates, c) GCD curves, d) EIS plots, e) Ragone plot, f) cycling stability plot and the inset is EIS curves after electrochemical cycling.

of cycles. This stability is attributed to the structural integrity and electrochemical activity of the material being maintained during cycling.

In summary, the 1:2:0.5(Co) sample exhibits superior performance in various electrochemical assessments, including cyclic voltammetry, charge-discharge (CP), electrochemical impedance spectroscopy, specific capacitance, and kinetic analysis compared to the other two material compositions. It demonstrates higher charge storage capacity, faster reaction kinetics, and excellent rate capability. The outstanding electrochemical performance is mainly attributed to the optimized composition ratio that refines the material's microstructure. To further evaluate the electrocatalytic performance of the three best-performing materials, systematic tests were conducted on their HER and OER performance under 1 M KOH conditions.

In a three-electrode system, as shown in Figure 8a, the LSV curves of the 2:1.5:0.5 (Ni), 1:2:0.5 (Co), and 2:1:1.5 (Ni,Co) samples, as well as the Pt/C reference material, are compared. The 1:2:0.5 (Co) sample exhibits the lowest overpotential of only 100.4 mV at a current density of -10 mA cm^{-2} (excluding the precious metal Pt/C), significantly outperforming the other two catalysts, indicating its higher HER activity. However, at 100 mA cm^{-2}, the overpotential of the 1:2:0.5 (Co) sample increases more rapidly, likely due to active site saturation or local dissolution, which limits rapid electron transfer. In contrast, the 2:1:1.5 (Ni,Co) sample with a higher Fe content shows superior activity at high current densities. This suggests that appropriately increasing the Fe content is a critical step to enhance the electrochemical performance of ternary metal hydroxide electrode materials. Figure 8b presents the Tafel slopes of the three materials. The 1:2:0.5 (Co) sample exhibits a Tafel slope of 71.2 mV dec^{-1}, which is lower than those of the 2:1:1.5 (Ni,Co) (90.9 mV dec^{-1}) and 2:1.5:0.5 (Ni) (100.5 mV dec^{-1}) samples. In alkaline electrolyte, the HER can be divided into three steps: the Volmer reaction, which corresponds to a Tafel slope of 120 mV dec^{-1}; the Heyrovsky reaction, typically exhibiting a slope of 40 mV dec^{-1}; and the Tafel reaction, with a slope of 30 mV dec^{-1}. The Tafel slope of 71.2 mV dec^{-1} for the 1:2:0.5 (Co) sample suggests that the HER mechanism follows the Volmer–Heyrovsky pathway, indicating faster reaction kinetics and a higher reaction rate. Figure 8c calculates the double-layer capacitance (Cdl) from CV curves at different scan rates, indirectly reflecting the specific surface area and number of active sites. The 1:2:0.5(Co) sample has the highest Cdl (0.0021 mF cm^{-2}), indicating the largest electrochemically active surface area beneficial for the HER process. Figure 8d presents the electrochemical impedance spectroscopy of the three materials, closely related to the charge transfer rate on the electrode surface. The smallest semicircle in the high-frequency region for the 1:2:0.5(Co) sample indicates the lowest interface charge transfer resistance and more efficient electron transport. Figure 8e compares the HER overpotentials of the three materials at different current densities. The 1:2:0.5(Co) sample's overpotentials at 10, 30, and 50 mA·cm^{-2} are 100.4 mV, 180.4 mV, and 236.8 mV, respectively, all lower than those of the other two compositions, further confirming its excellent HER activity. Subsequently, to evaluate the long-term stability of the 1:2:0.5 (Co) catalyst, a 90 h chronoamperometric test was conducted. As shown in Figure 8f, the current density

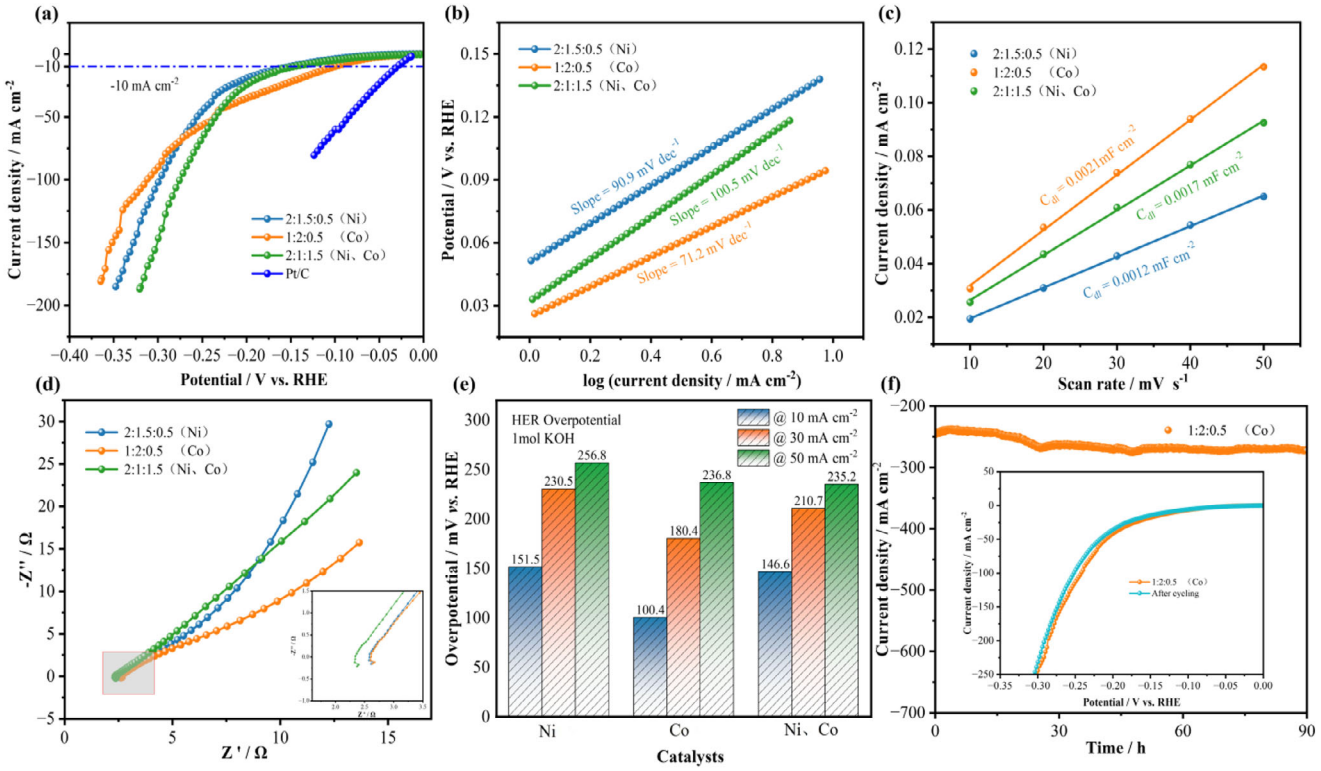

Figure 8. HER performances in 1 M KOH solutions a) Polarization curves at scan rate of 5 mV s^{-1}, b) Tafel plots, c) C_{dl} plots, d) Nyquist plots, e) overpotential at different current densities, f) chronoamperometric stability tests the inset is LSV curves after electrochemical cycling.

remained relatively excellent stability throughout the entire testing period. The inset presents a comparison of the LSV curves before and after the stability test, where the curves are nearly overlapping with only minor shifts, providing strong evidence that the catalyst retains its intrinsic electrocatalytic activity even after prolonged operation. This suggests great potential for practical applications. In addition, a 60 h stability test was also performed on the Pt/C electrode material (Figure S2a). During the entire 60 h continuous operation, the current density of the Pt/C electrode remained stable around −400 mA cm^{-2}, demonstrating excellent electrochemical stability even under high current density conditions. These results confirm that noble metal-based materials still exhibit superior performance in applications requiring high efficiency and long-term durability. Furthermore, as clearly observed in the SEM images shown in Figure S1, the NiCoFe-LDH catalyst nanosheets exhibit a distinct subsurface oxidation layer and a slightly expanded passivation interface on the outer surface. This observation suggests that the sample undergoes over-oxidation and passivation, which effectively prevents further oxidation and corrosion of the inner material. The synergistic effect of surface oxidation and passivation provides a plausible explanation for the excellent electrochemical stability and performance of the material during the cycling process. In terms of OER performance, the LSV curves (Figure 9a) at a scan rate of 2 mV s^{-1} show that the 2:1:1.5 (Ni,Co) sample has lower overpotentials compared to other catalysts. Specifically, at 10 mA cm^{-2} and 50 mA cm^{-2}, the overpotentials are 207.1 mV and 235.3 mV, respectively, significantly lower than other non-noble metal catalysts but still higher than IrO_2 (135.1 mV at 10 mA cm^{-2}). Additionally, the Ni-based substrate has an overpotential of 450 mV at 50 mA·cm^{-2}, contributing negligibly to the electrocatalytic performance. Figures 9b,c explore the reaction kinetics through Tafel plots and Cdl values, revealing that 2:1:1.5(Ni,Co) @51.9 mV dec^{-1} < 1:2:0.5(Co) @63.1 mV dec^{-1} < 2:1.5:0.5(Ni) @67.2 mV dec^{-1}, with the order of activity being 2:1:1.5(Ni,Co) 0.186 mF cm^{-2} > 1:2:0.5(Co) 0.141 mF cm^{-2} > 2:1.5:0.5(Ni) 0.099 mF cm^{-2}. This indicates that 2:1:1.5(Ni,Co) possesses superior reaction kinetics and electrochemical active surface area, providing more active sites for the OER process. Figure 9d shows the EIS spectra, where the 2:1:1.5(Ni,Co) sample has the smallest semicircle diameter in the high-frequency region, indicating lower impedance during charge transfer. Figure 9e presents a radar chart showcasing key parameters related to HER and OER performance, highlighting that the 2:1:1.5(Ni,Co) sample excels in anodic OER reactions, whereas the 1:2:0.5(Co) catalyst is better suited for cathodic HER reactions. As shown in Figure 9f, a chronopotentiometry test was conducted to evaluate the long-term stability of the catalyst. The catalyst demonstrated stable operation for up to 90 h at a low current density of 10 mA cm^{-2}, with the potential remaining nearly constant at approximately 1.55 V. Notably, even when the current density was increased to 50 mA cm^{-2}, the potential remained highly stable at around 1.59 V over an additional 90-h period, with no significant increase observed. This excellent stability is attributed to the formation of a protective surface passivation layer, which effectively prevents further corrosion and maintains the structural integrity of the material.[47] In Figure S2b, a 100-h chronopotentiometry test was also performed on

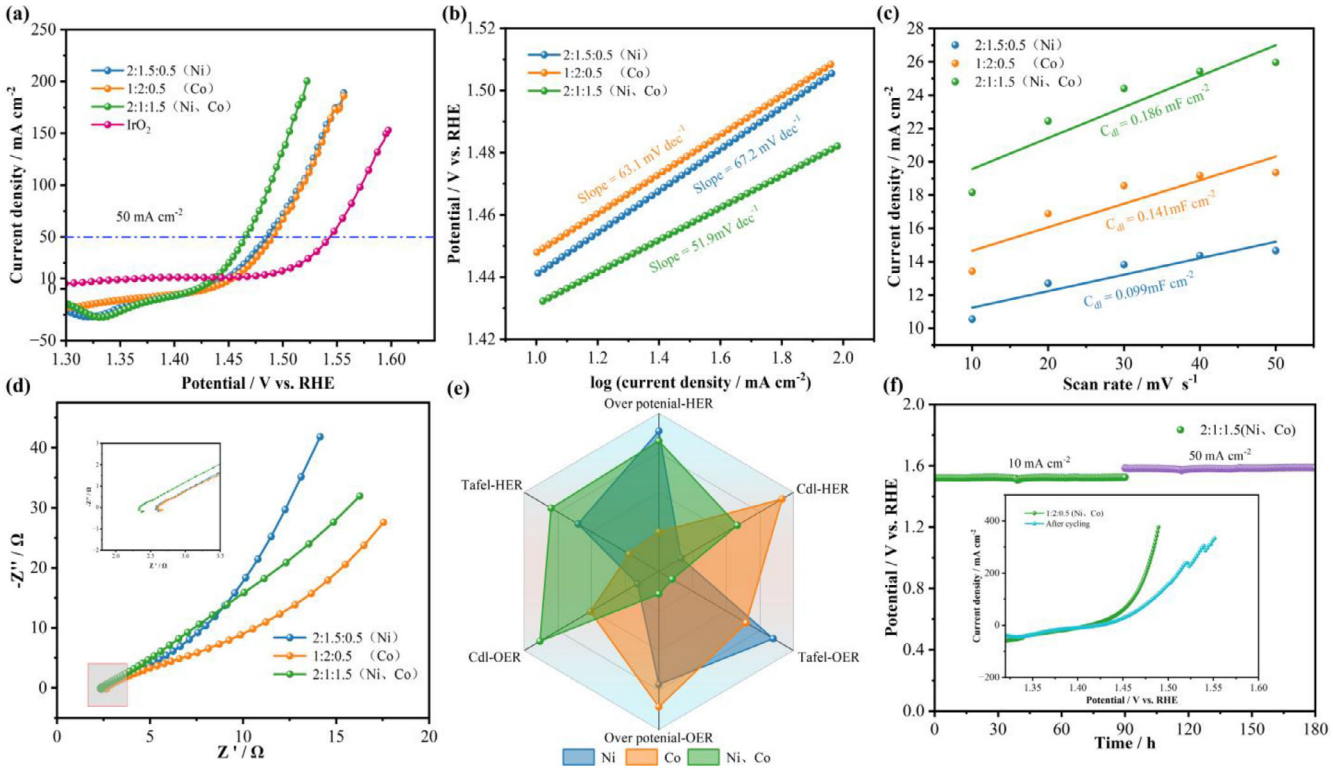

Figure 9. OER performances in 1 M KOH solutions a) polarization curves at scan rate of 2 mV s^{-1}, b) Tafel plots, c) C_{dl} plots, d) Nyquist plots, e) radar chart, f) chronopotentiometry stability tests the inset is LSV curves after electrochemical cycling.

Table 1. Comparison of NiCoFe electrocatalytic performance with previous literature reports.

Materials	Performances	Electrolyte	η(mV)	Refs.
NiCoFe-LDH	HER OER	1 M KOH	100.4 mV (10 mA cm^{-2}) 235.3 mV (50 mA cm^{-2})	This work
NiCoFe	HER	1 M KOH	90 mV (10 mA cm^{-2})	[48]
	OER		210 mV (10 mA cm^{-2})	
NiCoFe/NFF	OER	1 M KOH	200 mV (10 mA cm^{-2})	[49]
NiCoFe LDH	OER	1 M KOH	233 mV (50 mA cm^{-2})	[50]
Fe-NiCoSe	HER	1 M KOH	120 mV (10 mA cm^{-2})	[51]
Cr-Cu_2S @CF	HER	0.5 M H_2SO_4	225 mV (-100 mA cm^{-2})	[52]
Cu_2CoSnS_4	HER	0.5 M H_2SO_4	192.1 mV (-10 mA cm^{-2})	[53]

the noble metal IrO_2 catalyst. Throughout the entire testing period, the potential of the IrO_2 catalyst remained at 1.44 V (at 10 mA cm^{-2}), with almost no voltage degradation observed. This level of stability is crucial for practical water-splitting applications that require high efficiency and long operational lifetimes. Although the initial overpotential of our catalyst may be slightly higher than that of the expensive IrO_2, our non-noble metal-based catalyst offers a promising and sustainable alternative for practical OER applications. Table 1 compares the electrocatalytic performance of NiCoFe-LDH with previous literature reports, underscoring the superior electrocatalytic performance of the samples discussed.

To further explore the potential application value of the prepared electrocatalysts in overall water splitting, a two-electrode setup was used to test the performance of overall water electrolysis. The anode utilized the 2:1:1.5(Ni,Co) sample, while the cathode employed the 1:2:0.5(Co) catalyst. Figure 10a provides a schematic diagram of this setup. In Figure 10b, the distribution of relaxation times (DRT) curves at various potentials ranging from 1.636 V to 1.758 V is presented, where $\gamma(\tau)$ represents the impedance distribution corresponding to a specific time constant τ. DRT analysis enables the clear differentiation of electrochemical processes that are often indistinguishable using conventional electrochemical impedance spectroscopy (EIS).[54]

Table 2. Comparison of energy densities of NiCoFe-LDH SCc with previous literature reports.

Materials	Energy Density (Wh kg^{-1})	Power Density (W kg^{-1})	Refs.
NiCoFe-LDH	72.3	4050	This work
La@$NiCoFe_2O_4$	42.2	2207	[42]
$NiCo_2O_4$-Mn	19.9	3149	[43]
NiCo-PBA	42.16	9545.1	[44]
NiCoP	16.72	7250	[45]
NiCoZnS@NiCoFe-LDH	66.25	1500	[46]

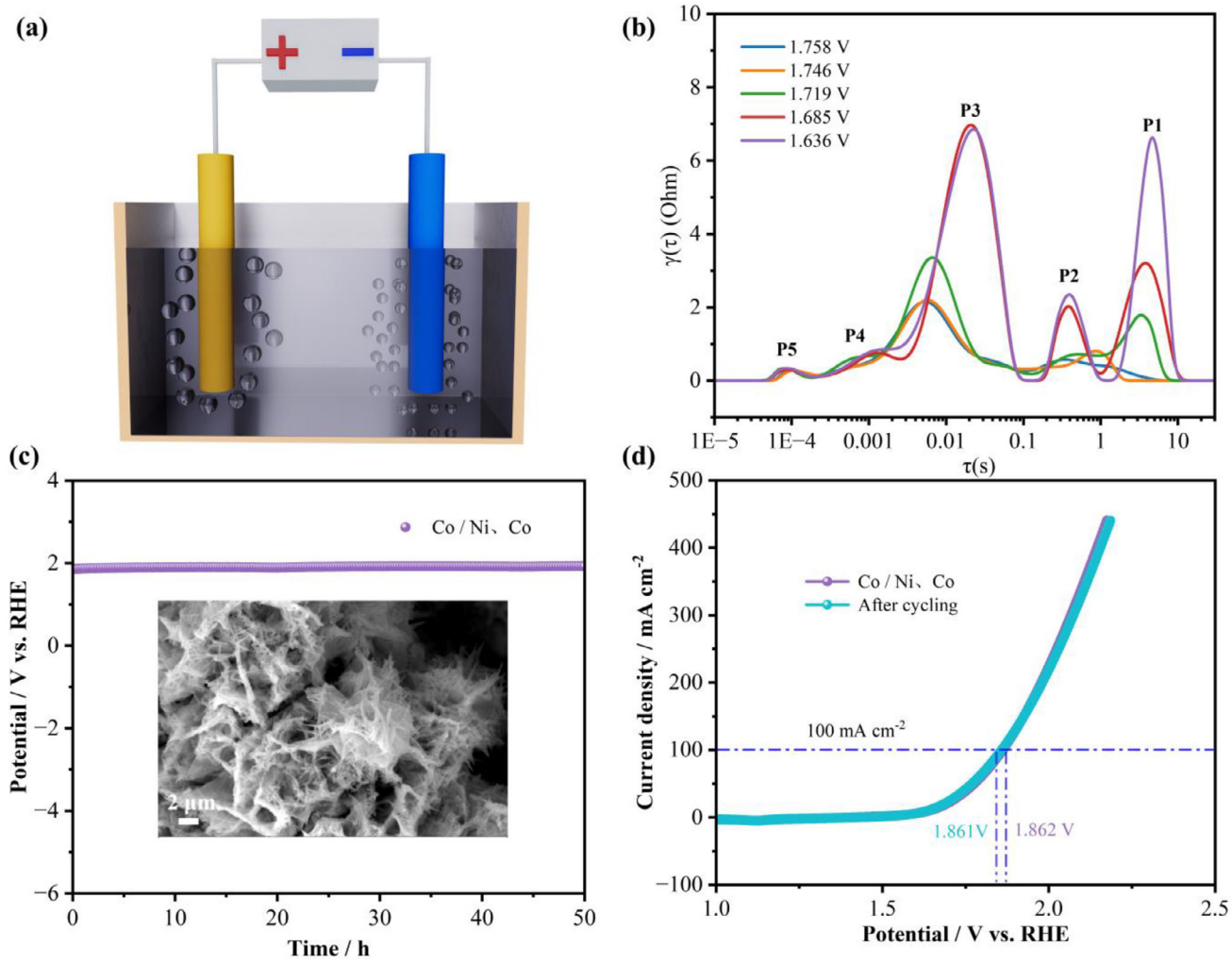

Figure 10. Overall water-splitting performance of the electrocatalysts a) device schematic diagram, b) distribution of relaxation times (DRT) curve, c) chronoamperometric stability tests the insets is SEM images of 1:2:0.5(Co), d) LSV curves before and after electrochemical cycling.

The DRT spectra reveal five distinct characteristic peaks (P1–P5), each corresponding to a unique electrochemical process. At lower potentials (e.g., 1.636 V), the P1 ($\gamma = 6.5\ \Omega$) and P3 peaks are most pronounced, indicating that the reaction kinetics are primarily limited by both mass transfer processes and the primary charge transfer step. The relatively weak P4 peak suggests that surface oxidation processes have only just begun at this stage. In the medium potential range (1.685–1.719 V), the intensity of the P2 peak increases, while the P3 peak remains significant, implying that the relaxation of adsorbed intermediates and charge transfer processes jointly influence the reaction kinetics. Additionally, the P4 peak becomes more prominent, especially at 1.719 V, indicating an acceleration in surface oxidation. Meanwhile, the gradual weakening of the P1 peak suggests a reduction in mass transfer limitations as the potential increases. At higher potentials (1.746–1.758 V),

the P1 peak nearly disappears, indicating that mass transfer is no longer a limiting factor. The P3 peak remains detectable but decreases in magnitude, reflecting a reduction in charge transfer impedance. The P4 peak significantly weakens, suggesting that the surface oxide layer has reached a stable state. The P2 peak maintains moderate intensity, highlighting the continued importance of intermediate adsorption/desorption processes even at elevated potentials. With increasing potential, the reaction mechanism gradually shifts from being dominated by mass transfer limitations (dominated by P1) to being co-controlled by charge transfer and surface adsorption processes (dominated by P2 and P3). Each characteristic peak corresponds to a distinct electrochemical process, effectively revealing the reaction kinetics of the sample under different potentials.[55–57] Figure 10c presents the stability test results of the NiCoFe catalyst. During continuous operation for 50 h, the dual-electrode material showed excellent stability with only minor fluctuations, confirming the structural stability and long-term activity of the catalyst under prolonged operational conditions. The inset shows an SEM image after the stability test. Figure 10d compares the LSV curves before and after the stability test, showing only a slight shift in voltage at a current density of 100 mA cm^{-2} after testing. The decomposition voltage remains as low as 1.861 V (without IR compensation), further confirming the excellent water-splitting performance of the material. This indicates not only the effectiveness but also the durability of the catalysts when applied in practical water-splitting applications.

4. Conclusion

In summary, we have successfully synthesized a series of NiCoFe ternary layered double hydroxide catalysts with unique nanosheet array structures via an innovative one-step hydrothermal method. Distinct from conventional approaches that often focus on a single performance aspect, we systematically elucidated the synergistic regulatory mechanism of iron in NiCo-based LDHs on both energy storage and electrocatalytic properties. For energy storage, the NiCoFe-LDH sample with a Ni:Co:Fe molar ratio of 1:2:0.5 exhibited optimal electrochemical performance, achieving a high specific capacitance of 860 $C{\cdot}g^{-1}$. The supercapacitor assembled using this material has a remarkable energy density of 72.3$Wh{\cdot}kg^{-1}$ at a power density of 4050 $W{\cdot}kg^{-1}$. Furthermore, it demonstrated outstanding cycling stability, retaining 69.2% of its initial capacitance after 7200 charge-discharge cycles. Beyond energy storage, this research further extended the application of NiCoFe-LDH to electrocatalytic water splitting. In an alkaline electrolyte, the catalyst showed excellent electrocatalytic activity for the HER, achieving a low overpotential of 100.4 mV at a current density of -10 $mA{\cdot}cm^{-2}$. We precisely tailored the Ni:Co:Fe ratio to 2:1:1.5 for another NiCoFe-LDH sample, which significantly optimized the electronic structure and active site configuration of the LDH to boost OER performance, exhibiting an impressive overpotential of 235.3 mV at 50 $mA{\cdot}cm^{-2}$. Moreover, when both optimized NiCoFe-LDH samples were simultaneously employed as anode and cathode in a symmetric two-electrode system for overall water splitting, the system required only a minimal cell voltage of 1.861 V to reach a current density of 100 $mA{\cdot}cm^{-2}$. This result powerfully underscores the robust catalytic synergy and exceptional efficiency achieved through rational component design of these materials for practical water-splitting applications. This study, through its original component design and refined synthesis conditions, provides profound mechanistic insights and universal guidance for understanding and enhancing the multifaceted electrochemical and catalytic performance of NiCoFe-LDH. These findings not only lay a solid foundation for the development of next-generation multifunctional materials that integrate high-performance energy storage and efficient catalytic conversion but also open vast prospects for their application in future advanced energy systems.

Acknowledgments

This work was supported by the Project of Education Department of Liaoning Province (No. LJKMZ20220959), the National Natural Science Foundation of China (No. 51971106).

Conflict of Interests

The authors declare no conflict of interest.

Data Availability Statement

The data that support the findings of this study are available on request from the corresponding author. The data are not publicly available due to privacy or ethical restrictions.

Keywords: Electrocatalysis · NiCoFe Layered Hydroxides · Supercapacitors · Water Splitting

[1] J. Liu, J. Wang, C. Xu, H. Jiang, C. Li, L. Zhang, Z. X. Shen, *Adv. Sci.* **2018**, *5*, 1700322.
[2] Y. Zhong, X. Deng, S. Zhan, J. Fang, R. Yu, J. Tu, *Adv. Energy Mater.* **2018**, *8*, 1701110.
[3] S. Deng, D. Chao, Y. Zhong, Y. Zeng, Z. Yao, J. Zhan, J. Tu, *Energy Storage Mater.* **2018**, *12*, 137–144.
[4] B. Y. Zhang, S. L. Xu, J. Li, H. Y. Zhou, X. Li, R. D. Zhao, P. D. Zhao, *CrystEngComm* **2015**, *27*, 3700–3711.
[5] Q. Song, C. Zheng, H. Chi, J. Zhang, Z. Ji, *Nanotechnology* **2016**, *28*, 055405.
[6] Q. Xie, P. Zhao, S. Wu, Y. Zhang, *J. Mater. Sci.* **2017**, *52*, 13478–13489.
[7] S. L. Xu, R. D. Zhao, R. Y. Li, J. Li, J. Wang, F. Y. Guo, F. F. Wu, *J. Mater. Chem. A* **2024**, *12*, 15950–15965.
[8] P. Sivakumar, J. Balamurugan, C. J. Raj, P. Subramanian, A. D. Savariraj, R. Manikandan, H. Jung, *J. Mater. Chem. A* **2025**, *13*, 5961–5973.
[9] P. Sivakumar, C. J. Raj, H. Jung, H. S. Park, *J. Energy Storage* **2023**, *69*, 107946.
[10] P. Sivakumar, M. G. Jung, C. J. Raj, J. Park, H. S. Park, H. Jung, *Int. J. Energy Res.* **2021**, *45*, 18091–18102.
[11] W. T. Hong, M. Risch, K. A. Stoerzinger, A. Grimaud, J. Suntivich, Y. Shao-Horn, *Energy Environ. Sci.* **2015**, *8*, 1404–1427.
[12] W. Zhu, R. Zhang, F. Qu, A. M. Asiri, X. Sun, *ChemCatChem* **2017**, *9*, 1721–1743.

[13] J. Suntivich, K. J. May, H. A. Gasteiger, J. B. Goodenough, Y. Shao-Horn, *Science* **2011**, *334*, 1383–1385.
[14] J. Wang, X. Ma, F. Qu, A. M. Asiri, X. Sun, *Inorg. Chem.* **2017**, *56*, 1041–1044.
[15] R. P. Patel, P. M. Pataniya, M. Patel, K. Joshi, K. H. Modi, P. Sahatiya, C. K. Sumesh, *Sol. Energy* **2022**, *246*, 343–354.
[16] P. M. Pataniya, C. K. Sumesh, *J. Electroanal. Chem.* **2022**, *912*, 116270.
[17] H. K. Thakkar, K. K. Joshi, P. M. Pataniya, G. Bhadu, S. Siraj, P. Sahatiya, C. K. Sumesh, *Int. J. Hydrogen Energy* **2023**, *48*, 38266–38278.
[18] K. K. Joshi, P. M. Pataniya, G. Bhadu, C. K. Sumesh, *Int. J. Hydrogen Energy* **2023**, *48*, 7260–7272.
[19] W. Chen, K. Song, L. Mi, X. Feng, J. Zhang, S. Cui, C. Liu, *J. Mater. Chem. A* **2017**, *5*, 10027–10038.
[20] B. J. Lee, S. R. Sivakkumar, J. M. Ko, J. H. Kim, S. M. Jo, D. Y. Kim, *J. Power Sources* **2007**, *168*, 546–552.
[21] F. Shi, L. Li, X. L. Wang, C. D. Gu, J. P. Tu, *RSC Adv.* **2014**, *4*, 41910–41921.
[22] J. Liu, S. Zhao, X. Wu, *Chin. Chem. Lett.* **2024**, *35*, 109059.
[23] S. Li, M. Zhao, Y. Xu, Z. Liu, M. Li, Q. Huang, X. Wu, *Chin. Chem. Lett.* **2025**, *36*, 110701.
[24] C. Zhao, Y. Liu, S. Li, X. Wu, J. Liu, *Chin. Chem. Lett.* **2025**, *36*, 110185.
[25] Y. Liu, X. Wang, Z. S. Wu, Y. R. Cho, X. Wu, *Adv. Funct. Mater.* **2025**, *25*, 2505535.
[26] M. Shao, R. Zhang, Z. Li, M. Wei, D. G. Evans, X. Duan, *Chem. Commun.* **2015**, *51*, 15880–15893.
[27] D. Zhao, K. Jiang, Y. Pi, X. Huang, *ChemCatChem* **2017**, *9*, 84–88.
[28] Z. Lu, L. Qian, Y. Tian, Y. Li, X. Sun, X. Duan, *Chem. Commun.* **2016**, *52*, 908–911.
[29] H. Chen, J. Jiang, Y. Zhao, L. Zhang, D. Guo, D. Xia, *J. Mater. Chem. A* **2015**, *3*, 428–437.
[30] M. K. Bates, Q. Jia, H. Doan, W. Liang, S. Mukerjee, *ACS Catal.* **2016**, *6*, 155–161.
[31] X. Zheng, Z. Gu, Q. Hu, B. Geng, X. Zhang, *RSC Adv.* **2015**, *5*, 17007–17013.
[32] H. Chen, L. Hu, M. Chen, Y. Yan, L. Wu, *Adv. Funct. Mater.* **2014**, *24*, 934–942.
[33] L. Liu, X. Hu, H. Y. Zeng, M. Y. Yi, S. G. Shen, S. Xu, X. Cao, J. Z. Du, *J. Mater. Sci. Technol.* **2019**, *35*, 1691–1699.
[34] P. Sivakumar, C. J. Raj, A. D. Savariraj, R. Manikandan, R. Rajendran, H. Jung, *Surf. Interfaces* **2024**, *51*, 104629.
[35] A. Guzmán-Vargas, J. Vazquez-Samperio, M. A. Oliver-Tolentino, N. Nava, N. Castillo, M. J. Macías-Hernández, E. Reguera, *J. Mater. Sci.* **2018**, *53*, 4515–4526.
[36] X. Xu, J. Liu, Z. Liu, J. Shen, R. Hu, J.-W. Liu, L. Ouyang, L. Zhang, M. Zhu, *ACS Nano* **2017**, *11*, 9033–9040.
[37] L. Ye, Z. Bao, Y. Zhao, L. Zhao, *RSC Adv.* **2018**, *8*, 23817–23824.
[38] M. Guo, Y. Lin, L. Zhao, *J. Alloys Compd.* **2021**, *850*, 156787.
[39] J. Shang, Y. Zhang, Q. Zhang, Y. Li, F. Deng, R. Gao, J. Wang, *J. Alloys Compd.* **2022**, *925*, 166668.
[40] E. Elanthamilan, S. F. Wang, *Batteries Supercaps* **2025**, e202400754.
[41] C. X. Zhao, J. N. Liu, B. Q. Li, D. Ren, X. Chen, J. Yu, Q. Zhang, *Adv. Funct. Mater.* **2020**, *30*, 2003619.
[42] Y. Guo, T. Chen, Y. Zou, *Materials* **2023**, *16*, 1643.
[43] K. Kowsuki, R. Navamathavan, *Surf. Interfaces* **2025**, *56*, 105641.
[44] G. Liu, G. Wang, Z. J., *Electrochim. Acta* **2024**, *502*, 144832.
[45] Z. Zhao, Y. Miao, Q. Lu, *J. Power Sources* **2024**, *606*, 234587.
[46] S. B. Lv, H. Y. Zeng, K. M. Zou, S. Xu, Y. W. Long, H. B. Li, Z. Li, *Dalton Trans.* **2021**, *50*, 11542–11554.
[47] M. Wang, X. Liu, X. Wu, *Nano Energy* **2023**, *114*, 108681.
[48] G. H. El-Nowihy, M. M. Abdellatif, M. S. El-Deab, *Renew. Energy* **2024**, *226*, 120395.
[49] H. Zhou, Y. Zhang, C. Shi, K. Yuan, R. Zhou, P. Zhao, Y. Wang, *J. Colloid Interface Sci.* **2024**, *663*, 725–734.
[50] C. Su, D. Wang, W. Wang, N. Mitsuzaki, R. Shao, Q. Xu, Z. Chen, *J. Electroanal. Chem.* **2024**, *960*, 118167.
[51] D. Wang, L. Wang, G. Liang, H. Li, Z. Liu, Z. Tang, C. Zhi, *ACS Nano* **2019**, *13*, 10643–10652.
[52] N. Trivedi, K. K. Joshi, S. Siraj, P. Sahatiya, V. Patel, C. K. Sumesh, P. M. Pataniya, *Int. J. Hydrogen Energy* **2024**, *49*, 1113–1122.
[53] K. K. Joshi, P. M. Pataniya, G. R. Bhadu, C. K. Sumesh, *Int. J. Hydrogen Energy* **2024**, *49*, 829–842.
[54] A. Maradesa, B. Py, J. Huang, Y. Lu, P. Iurilli, A. Mrozinski, F. Ciucci, *Joule*, **2024**, *8*, 2505535.
[55] B. Chang, Y. Ren, N. Mu, S. Zuo, C. Zou, W. Zhou, H. Zhang, *Adv. Mater.* **2025**, *37*, 2405447.
[56] C. Plank, T. Rüther, L. Jahn, M. Schamel, J. P. Schmidt, F. Ciucci, M. A. Danzer, *J. Power Sources* **2024**, *594*, 233845.
[57] X. Huo, G. Shan, L. Yang, L. Abrar, L. Gao, W. Li, J. Zhang, *Int. J. Hydrogen Energy* **2024**, *91*, 693–702.

Manuscript received: June 10, 2025
Revised manuscript received: July 30, 2025
Version of record online: ■■, ■■